RAA 2017 Vol. **17** No. **7**, 70 (10pp) doi: 10.1088/1674–4527/17/7/70

http://www.raa-journal.org *http://iopscience.iop.org/raa*

***R**esearch in*
***A**stronomy and*
***A**strophysics*

Surface thermophysical properties on the potentially hazardous asteroid (99942) Apophis

Liang-Liang Yu[1,2], Jianghui Ji[2] and Wing-Huen Ip[1,3]

[1] Space Science Institute, Macau University of Science and Technology, Taipa, Macau, China; *yullmoon@live.com*
[2] CAS Key Laboratory of Planetary Sciences, Purple Mountain Observatory, Chinese Academy of Sciences, Nanjing 210008, China; *jijh@pmo.ac.cn*
[3] Institute of Astronomy, National Central University, Zhongli, Taoyuan 32049; *wingip@astro.ncu.edu.tw*

Received 2017 January 8; accepted 2017 March 15

Abstract We investigate the surface thermophysical properties (thermal emissivity, thermal inertia, roughness fraction and geometric albedo) of asteroid (99942) Apophis, using the currently available mid-infrared observations from CanariCam on Gran Telescopio CANARIAS and far-infrared data from PACS on Herschel, based on the Advanced Thermophysical Model. We show that the thermal emissivity of Apophis should be wavelength dependent from $8.70\,\mu$m to $160\,\mu$m, and the maximum emissivity may appear around $20\,\mu$m, similar to that of Vesta. Moreover, we further derive the thermal inertia, roughness fraction, geometric albedo and effective diameter of Apophis within a possible 1σ scale of $\Gamma = 100^{+100}_{-52}\,\mathrm{J m^{-2}\,s^{-0.5}\,K^{-1}}$, $f_\mathrm{r} = 0.78 \sim 1.0$, $p_\mathrm{v} = 0.286^{+0.030}_{-0.026}$ and $D_\mathrm{eff} = 378^{+19}_{-25}\,\mathrm{m}$, and 3σ scale of $\Gamma = 100^{+240}_{-100}\,\mathrm{J m^{-2}\,s^{-0.5}\,K^{-1}}$, $f_\mathrm{r} = 0.2 \sim 1.0$, $p_\mathrm{v} = 0.286^{+0.039}_{-0.029}$ and $D_\mathrm{eff} = 378^{+27}_{-29}\,\mathrm{m}$. The derived low thermal inertia but high roughness fraction may imply that Apophis could have regolith on its surface, where stronger space weathering but weaker regolith migration has happened in comparison with asteroid Itokawa. Our results show that small-size asteroids could also have fine regolith on the surface, and further infer that Apophis may have been delivered from the Main Belt by the Yarkovsky effect.

Key words: techniques: thermal infrared — variables: thermal inertia — asteroid: individual: (99942) Apophis

1 INTRODUCTION

(99942) Apophis (2004 MN4) is categorized as an Aten-group near-Earth asteroid based on its orbital characteristics. The asteroid was identified as a potentially hazardous object with a significant Earth impact probability of 2% in 2029, based on observations from December 2004 reported by JPL-Sentry and ESA-NEODyS. On 2004 December 27, the Spacewatch survey announced pre-discovery observations (Gilmore et al. 2004) that were acquired starting from March 2004, and negated any possibility of impact with Earth in 2029.

Radar observations of Apophis were obtained by the Arecibo observatory in January 2005, August 2005 and May 2006. More recently, Thuillot et al. (2015) reported new astrometric observations obtained by space-based *Gaia-FUN-SSO* during Apophis' latest period of visibility from 2012 December 21 to 2013 February 5, and soon afterwards, Wang et al. (2015) published precise 298 CCD position data observed by the ground-based 2.4-m telescope administered by Yunnan Observatories from 2013 February 4 to 2013 March 2. These observations significantly reduced Apophis' orbital uncertainty and led to a more accurate estimation of the distance during the encounter of about 5-6 Earth radii from the geocenter in 2029 (Giorgini et al. 2008; Thuillot et al. 2015; Wang et al. 2015). Although the possibility of an impact in 2029 has been eliminated, other potential impacts may still exist in following decades.

Chesley (2006) showed that the Yarkovsky effect (Bottke et al. 2006) significantly affects post-2029 predictions of Apophis' orbit evolution and thus should be taken into account for its impact predictions. As is well known, the Yarkovsky effect due to the recoil of reflected

and thermally emitted photons is one of the most important non-gravitational effects on asteroids. Utilizing selected best astrometric and radar data covering the interval from 2004 March 15 to 2012 December 29, Farnocchia et al. (2013) carried out a detailed orbital analysis and quantitatively verified that predictions of Apophis impacting Earth between 2060 and 2105 are sensitive to its physical parameters, including diameter, albedo, rotation period, obliquity, density and thermal inertia, which determine the rate of Yarkovsky drift for Apophis' semimajor axis. In addition, Vokrouhlický et al. (2015) provided a more advanced estimation of Apophis' Yarkovsky effect, and predicted that Apophis' secular change in the semimajor axis may be $(-12.8 \pm 3.6) \times 10^{-4}\,\mathrm{AU\,Myr^{-1}}$. Therefore, accurate thermal properties (thermal inertia, roughness fraction and so on) and shape model are necessary to predict its Earth impact probability in the following decades in consideration of the significance played by the Yarkovsky effect.

By comparing spectral and mineralogical characteristics of likely meteorite analogs from 0.55 to 2.45 μm reflectance spectral measurements of Apophis observed by the NASA IRTF and the Baade Telescope at the Magellan Observatory, Binzel et al. (2009) found that Apophis appears well classified as an Sq-type and most closely resembles LL ordinary chondrite meteorites, which is rather similar to asteroid Itokawa (Abe et al. 2006).

With the photometric observations of Apophis from December 2012 to April 2013, Pravec et al. (2014) showed Apophis has a non-principle axis rotation, and reconstructed its convex shape model, where the retrograde rotation period is $P_1 = 30.56\,\mathrm{h}$ and the spin axis orientation is $(-75.0^\circ, 250.0^\circ)$. Pravec et al. (2014) also derived Apophis' average absolute visual magnitude to be $H_\mathrm{v} = 19.09$ assuming the slope parameter to be $G = 0.24 \pm 0.11$.

Generally, the thermal inertia of an asteroid can be evaluated by fitting infrared (IR) observations with a thermophysical model to reproduce thermal emission curves. Following the shape model of Pravec et al. (2014), Müller et al. (2014) utilized the so-called thermophysical model (TPM) to analyze Apophis' Herschel-far-IR observations, and derived its thermal inertia to be $250 - 800\,\mathrm{Jm^{-2}\,s^{-0.5}\,K^{-1}}$ with a best solution of about $600\,\mathrm{Jm^{-2}\,s^{-0.5}\,K^{-1}}$, mean effective diameter of $375^{+14}_{-10}\,\mathrm{m}$, and geometric albedo of $0.30^{+0.05}_{-0.06}$. All these properties of Apophis are very similar to those of Itokawa (Müller et al. 2005; Fujiwara et al. 2006), indicating that Apophis might also have a rubble-pile structure. However, recently Licandro et al. (2016) derived a relatively lower thermal inertia of $50 - 500\,\mathrm{Jm^{-2}\,s^{-0.5}\,K^{-1}}$ with a best solution of $\Gamma = 150\,\mathrm{Jm^{-2}\,s^{-0.5}\,K^{-1}}$ and low surface roughness, indicating surface material like that of Eros. Licandro et al. (2016) used the same TPM as Müller et al. (2014), but added three new mid-IR data measured by CanariCam on Gran Telescopio CANARIAS. Both the work of Müller et al. (2014) and Licandro et al. (2016) assumed constant thermal emissivity to derive surface thermophysical properties, but actually thermal emissivity may be wavelength dependent from mid-IR to far-IR (Mueller & Lagerros 1998), which should be taken into account when deriving the surface thermophysical properties.

In the present work, we utilize the independently developed thermophysical simulation codes (Yu et al. 2014; Yu & Ji 2015) based on the framework of the Advanced Thermophysical Model (ATPM) (Rozitis & Green 2011) to analyze the mid-IR and far-IR data of Apophis observed by CanariCam and Herschel respectively. We show that if wavelength dependent emissivities are used, better solutions can be obtained, and the derived thermal inertia and effective diameter can be different from the results derived on the basis of constant emissivity (CE). Moreover, we find that the surface of Apophis may be a highly rough surface with low thermal inertia materials. The low thermal inertia of the small-size asteroid Apophis reveals that small-size asteroids may also have regolith on the surface, and further suggests that Apophis may have been delivered from the Main Belt by the Yarkovsky effect.

2 THERMOPHYSICAL MODELING

2.1 Thermal Infrared Observations

Until now, the available IR measurements of Apophis were far-IR data observed by the Herschel Space Observatory (Müller et al. 2014), and three mid-IR data measured by CanariCam on Gran Telescopio CANARIAS (Licandro et al. 2016). All data used in this work will be compared with the theoretical flux simulated from the so-called ATPM so as to derive the possible scale of surface thermophysical properties. We tabulate data used in the fitting in Table 1.

2.2 Advanced Thermophysical Model

In the ATPM (Rozitis & Green 2011; Yu et al. 2014; Yu & Ji 2015), we treat an asteroid as a polyhedron composed of N triangular facets. For each facet, the roughness is modeled by a fractional coverage of hemispherical micro-craters, denoted by f_r ($0 \leq f_\mathrm{r} \leq 1$), whereas the remaining fraction, $1 - f_\mathrm{r}$, represents a

Table 1 Observational Data used in This Work (Müller et al. 2014; Licandro et al. 2016)

Date (UT)	Wavelength (μm)	Flux (mJy)	$r_{\rm helio}$ (AU)	$\Delta_{\rm obs}$ (AU)	α (°)	Observation instrument
2013–01–06 00:10	70.0	36.3±1.1	1.03593	0.096247	+60.44	Herschel/PACS
2013–01–06 00:10	160.0	8.7±3.3	1.03593	0.096247	+60.44	Herschel/PACS
2013–01–06 00:44	100.0	22.8±1.7	1.03599	0.096234	+60.40	Herschel/PACS
2013–01–06 00:44	160.0	7.4±3.8	1.03599	0.096234	+60.40	Herschel/PACS
2013–01–06 01:15	70.0	37.5±1.3	1.03604	0.096221	+60.36	Herschel/PACS
2013–01–06 01:15	160.0	9.8±2.5	1.03604	0.096221	+60.36	Herschel/PACS
2013–01–06 01:47	100.0	25.0±1.5	1.03609	0.096208	+60.32	Herschel/PACS
2013–01–06 01:47	160.0	8.2±2.2	1.03609	0.096208	+60.32	Herschel/PACS
2013–03–14 06:40	70.0	12.6±2.7	1.093010	0.232276	–61.38	Herschel/PACS
2013–03–14 06:54	70.0	11.4±2.7	1.093003	0.232307	–61.38	Herschel/PACS
2013–03–14 07:07	70.0	10.4±2.7	1.092996	0.232338	–61.39	Herschel/PACS
2013–03–14 07:21	70.0	12.5±2.6	1.092989	0.232368	–61.39	Herschel/PACS
2013–03–14 07:35	70.0	13.3±2.7	1.092983	0.232397	–61.40	Herschel/PACS
2013–03–14 07:49	70.0	12.4±2.6	1.092976	0.232427	–61.40	Herschel/PACS
2013–01–29 22:04	12.5	240.0±20	1.079706	0.113407	–31.73	CanariCam/GTC
2013–01–29 23:09	17.65	310.0±70	1.079761	0.113478	–31.74	CanariCam/GTC
2013–01–29 23:52	8.70	140.0±10	1.079816	0.113549	–31.75	CanariCam/GTC

smooth flat surface. For such a rough surface facet, conservation of energy leads to an instant heat balance between sunlight, thermal emission, heat conduction, multiply-scattered sunlight and thermally-radiated fluxes from other facets. If each facet is small enough and far larger than the spatial scale of roughness, heat conduction in that region can be approximatively described as one-dimensional heat conduction. Meanwhile, the temperature T_i of each facet varies with time as the asteroid rotates. In this process, T_i can be significantly affected by shading, multiply-scattered sunlight and thermally-radiated fluxes from other facets, which explains the so-called thermal IR beaming effect well. When the entire asteroid comes into the final state of thermal equilibrium, T_i will change periodically following the rotation of the asteroid. Therefore, we can build numerical codes to simulate T_i at any rotation phase for the asteroid. For a given observation epoch, ATPM can reproduce a theoretical profile for each observed flux as

$$F_{\rm model}(\lambda) = \sum_{i=1}^{N} \epsilon(\lambda) S(i) f(i) B(\lambda, T_i) \ , \tag{1}$$

where $\epsilon(\lambda)$ is the monochromatic emissivity at wavelength λ, $S(i)$ is the area of facet i, $f(i)$ is a factor related to the view of facet i with respect to the telescope defined by

$$f(i) = v_i \frac{\boldsymbol{n}_i \cdot \boldsymbol{n}_{\rm obs}}{\pi \Delta^2}, \tag{2}$$

such that $v_{\rm i} = 1$ indicates facet i is visible (otherwise $v_{\rm i} = 0$), and $B(\lambda, T_i)$ is the Planck function

$$B(\lambda, T_i) = \frac{2\pi hc^2}{\lambda^5} \frac{1}{\exp\left(\frac{hc}{\lambda k T_i}\right) - 1} \ . \tag{3}$$

Thus the calculated $F_{\rm model}$ can be compared with the thermal IR fluxes summarized in Table 1 derived from the fitting process.

2.3 Fitting Procedure

In order to derive the thermophysical properties of Apophis via the ATPM procedure, several physical parameters are needed, including the three-dimensional (3D) shape model, effective diameter $D_{\rm eff}$ and the so-called thermal parameter

$$\Phi = \frac{\Gamma \sqrt{\omega}}{\varepsilon \sigma T_{\rm eff}^3} \ , \tag{4}$$

where ω is rotation frequency, Γ is thermal inertia, ε is averaged thermal emissivity over the entire emission spectrum and

$$T_{\rm eff} = \left[\frac{(1 - A_{\rm B}) F_\odot}{\varepsilon \sigma d_\odot^2} \right]^{1/4} \ ,$$

is effective temperature. The rotation frequency ω can be easily determined from light curves, while thermal inertia Γ is the parameter of interest which would be treated as a free parameter in the fitting procedure.

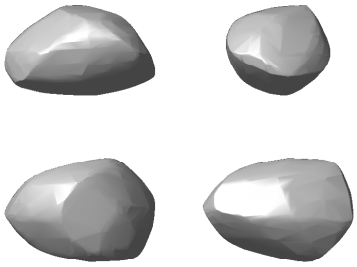

Fig. 1 The 3D shape model of Apophis utilized in this work is the light curve inversion shape reconstructed from Pravec et al. (2014).

We can employ the light curve inversion 3D shape model of Apophis reconstructed from Pravec et al. (2014) (Figure 1) in our fitting procedure.

According to Fowler & Chillemi (1992), an asteroid's effective diameter $D_{\rm eff}$, defined by the diameter of a sphere with a volume identical to that of the shape model, can be related to its geometric albedo p_v and absolute visual magnitude H_v via

$$D_{\rm eff} = \frac{1329 \times 10^{-H_v/5}}{\sqrt{p_v}} \,({\rm km}) \,. \tag{5}$$

In addition, geometric albedo p_v is related to the effective Bond albedo $A_{\rm eff,B}$ by

$$A_{\rm eff,B} = p_v q_{\rm ph} \,, \tag{6}$$

where $q_{\rm ph}$ is the phase integral that can be approximated by (Bowell et al. 1989)

$$q_{\rm ph} = 0.290 + 0.684G \,, \tag{7}$$

in which G is the slope parameter in the H, G magnitude system of Bowell et al. (1989). We use $H_{\rm v} = 19.09 \pm 0.19$, $G = 0.24 \pm 0.11$ and the results of Pravec et al. (2014) in the fitting procedure.

On the other hand, the asteroid's effective Bond albedo is the averaged result of both albedos of the smooth and rough surfaces, which can be expressed by the following relationship

$$A_{\rm eff,B} = (1 - f_{\rm r}) A_B + f_{\rm r} \frac{A_B}{2 - A_B} \,, \tag{8}$$

where A_B is the Bond albedo of a smooth Lambertian surface, which should be related to the composition of surface materials. Thus an input roughness fraction $f_{\rm r}$ and geometric albedo $p_{\rm v}$ can lead to a unique Bond albedo A_B and effective diameter $D_{\rm eff}$ to be used to fit the observations.

Then we have three free parameters — thermal inertia, roughness fraction and geometric albedo (or effective diameter) that can be extensively investigated in the fitting process. Other parameters are listed in Table 2.

Table 2 Assumed Physical Parameters used in ATPM

Property	Value	Reference
Number of vertices	1014	Pravec et al. (2014)
Number of facets	2024	Pravec et al. (2014)
Shape (a:b:c)	1.1135:1.0534:1	Pravec et al. (2014)
Angular momentum vector	$(-75.0^\circ, 250.0^\circ)$	Pravec et al. (2014)
Spin period	30.56 h	Pravec et al. (2014)
Absolute magnitude	19.09 ± 0.19	Pravec et al. (2014)
Slope parameter	0.24 ± 0.11	Pravec et al. (2014)
Thermal emissivity	0.9	assumption

It should also be noticed here that the utilized observational data are observed at various wavelengths from mid-IR to far-IR, thus it may no longer be suitable to assume an average CE for all wavelengths when calculating flux by Equation (1), because the spectral emissivity may differ with wavelength from mid-IR to far-IR (Mueller & Lagerros 1998). Therefore, the spectral emissivity ϵ remains a free parameter as well.

For the input free parameters, we use an initial geometric albedo $p_{\rm v} = 0.3$, but scan thermal inertia Γ in the range $0 \sim 500\,{\rm J m^{-2}\,s^{-0.5}\,K^{-1}}$, and roughness fraction $f_{\rm r}$ in the range $0.0 \sim 1.0$. For the spectral emissivity ϵ, we firstly assume it to have CE of 0.9, then vary it to see if we can get better solutions. For each pair of (Γ, $f_{\rm r}$), we could find a new $p_{\rm v}$ (or $D_{\rm eff}$) that gives a minimum reduced χ^2 defined as

$$\chi^2_{\rm r} = \frac{1}{n-3} \sum_{i=1}^{n} \Big[\frac{F_{\rm model}(\lambda_i, \Gamma, f_{\rm r}, p_{\rm v}) - F_{\rm obs}(\lambda_i)}{\sigma_{\lambda_i}} \Big]^2 \,, \tag{9}$$

which is used to assess the fitting degree of our model with respect to observations. Herein, the predicted model flux $F_{\rm model}$ is a rotationally averaged profile assuming rotation is along the angular momentum vector, for the rotation phases of Apophis at the time of observation are uncertain due to its non-principal axis rotation. Through the rotationally averaged procedure, the influence arising from the tumbling rotation would somewhat decrease, but the thermal properties can be revealed well from the effect of seasons, because we have observations at different epochs.

3 ANALYSIS AND RESULTS

As mentioned above, we firstly assume the spectral emissivity to be constant 0.9 for each observed wavelength, and obtain the reduced $\chi^2_{\rm r}$ for each input Γ and $f_{\rm r}$ (shown in Table 3).

From Table 3, we can see that low thermal inertia and high roughness fraction tend to fit the observations better; the best-fit solution, corresponding to the

Table 3 ATPM Fitting Results to Observations with Constant Spectral Emissivity $= 0.9$ for Each Wavelength

Roughness	Thermal inertia Γ ($\mathrm{Jm^{-2}\,s^{-0.5}\,K^{-1}}$)													
fraction	0		50		100		150		200		250		300	
$f_{\rm R}$	$p_{\rm v}$	$\chi^2_{\rm r}$	$p_{\rm v}$	$\chi^2_{\rm r}$	$p_{\rm v}$	$\chi^2_{\rm r}$	$p_{\rm v}$	$\chi^2_{\rm r}$	$p_{\rm v}$	$\chi^2_{\rm r}$	$p_{\rm v}$	$\chi^2_{\rm r}$	$p_{\rm v}$	$\chi^2_{\rm r}$
0.00	0.316	4.64	0.342	5.49	0.346	5.94	0.347	6.33	0.347	6.70	0.347	7.08	0.347	7.42
0.05	0.313	4.46	0.335	5.28	0.338	5.73	0.339	6.12	0.339	6.49	0.339	6.88	0.339	7.23
0.10	0.312	4.29	0.335	5.08	0.337	5.53	0.338	5.92	0.338	6.29	0.338	6.68	0.338	7.04
0.15	0.312	4.12	0.334	4.89	0.337	5.33	0.337	5.72	0.337	6.10	0.337	6.49	0.337	6.86
0.20	0.311	3.97	0.333	4.70	0.336	5.13	0.336	5.52	0.336	5.90	0.336	6.31	0.336	6.67
0.25	0.310	3.84	0.333	4.53	0.335	4.95	0.336	5.34	0.335	5.72	0.335	6.12	0.335	6.49
0.30	0.310	3.71	0.332	4.36	0.334	4.77	0.335	5.15	0.334	5.53	0.334	5.94	0.334	6.32
0.35	0.309	3.60	0.331	4.20	0.333	4.59	0.334	4.98	0.333	5.36	0.333	5.77	0.333	6.15
0.40	0.308	3.49	0.330	4.04	0.332	4.43	0.333	4.80	0.332	5.18	0.332	5.60	0.332	5.98
0.45	0.307	3.40	0.330	3.89	0.331	4.27	0.332	4.64	0.331	5.01	0.331	5.43	0.331	5.82
0.50	0.306	3.32	0.329	3.75	0.330	4.11	0.330	4.48	0.330	4.85	0.330	5.27	0.329	5.65
0.55	0.305	3.25	0.328	3.62	0.329	3.96	0.329	4.32	0.329	4.69	0.328	5.11	0.328	5.50
0.60	0.304	3.19	0.326	3.49	0.328	3.82	0.328	4.17	0.327	4.54	0.327	4.95	0.326	5.34
0.65	0.303	3.14	0.325	3.37	0.327	3.68	0.326	4.02	0.326	4.39	0.326	4.80	0.325	5.19
0.70	0.302	3.10	0.324	3.26	0.325	3.55	0.325	3.88	0.324	4.24	0.324	4.65	0.323	5.04
0.75	0.300	3.07	0.323	3.15	0.324	3.43	0.323	3.75	0.323	4.10	0.322	4.51	0.322	4.90
0.80	0.299	3.05	0.321	3.05	0.322	3.31	0.322	3.61	0.321	3.96	0.321	4.37	0.320	4.76
0.85	0.297	3.05	0.319	2.96	0.320	3.19	0.320	3.49	0.319	3.83	0.319	4.23	0.318	4.62
0.90	0.296	3.05	0.318	2.87	0.319	3.08	0.318	3.37	0.317	3.70	0.317	4.10	0.316	4.48
0.95	0.294	3.06	0.316	2.79	0.317	2.98	0.316	3.25	0.315	3.57	0.315	3.97	0.314	4.35
1.00	0.290	3.08	0.318	2.71	0.319	2.88	0.318	3.14	0.317	3.45	0.316	3.84	0.315	4.22

lowest reduced $\chi^2_{\rm r}$, appears at about $p_{\rm v} = 0.318$, $\Gamma = 50\,\mathrm{Jm^{-2}\ s^{-0.5}\ K^{-1}}$ and $f_{\rm r} = 1.0$. With this result, we plot the ratio of 'observation/model' to examine how these theoretical model results match the observations at various wavelengths (Fig. 2).

In Figure 2, we can see that the ratios at each wavelength are not randomly distributed around 1.0, but reveal a wavelength dependent feature like the red fitting curve, where the maximum ratio may appear around 20 μm. This feature implies that the spectral emissivity used in Equation (1) should not be a constant $\epsilon(\lambda) \equiv 0.9$, but should be wavelength dependent, where the maximum emissivity may occur around 20 μm. Thus we should introduce a wavelength dependent spectral emissivity $\epsilon(\lambda)$ to do the fitting process again.

Mueller & Lagerros (1998) reported the wavelength dependent spectral emissivity of asteroids Ceres and Vesta. As the spectral feature of Vesta may be much closer to Apophis than Ceres, we imagine that Apophis' emissivity changes with wavelength in a similar way to that of asteroid Vesta (Mueller & Lagerros 1998) as shown in Table 4. With this wavelength dependent emissivity, we derive better solutions.

Table 5 summarizes the reduced $\chi^2_{\rm r}$ obtained from each input pair of thermal inertia and roughness fraction when using the emissivity given in Table 4. We can see that, in this case, the high roughness fraction tends to fit better as well. But the best-fit thermal inertia and

Table 4 Assumed Emissivity for Different Wavelength

Wavelength (μm)	Emissivity
8.7, 12.5	0.90
17.65	0.96
70, 100	0.80
160	0.75

geometric albedo shift to $\Gamma = 100\,\mathrm{Jm^{-2}\,s^{-0.5}\,K^{-1}}$ and $p_{\rm v} = 0.286$ respectively. We compare the reduced $\chi^2_{\rm r}$ obtained from the two cases of CE and wavelength dependent emissivity (WDE) in Figure 3, where the black curves represent the reduced χ^2 obtained from CE input while the red curves stand for WDE. We can see that the obtained minimum reduced $\chi^2_{\rm r}$ can be significantly lower when the WDE is used to fit observations, indicating that the spectral emissivity of Apophis should be wavelength dependent.

Since we cannot obtain the best solutions by assuming CE, we have no reason to fit the observations with ATPM by using CE. Therefore, we adopt the WDE similar to that of asteroid Vesta to further derive the surface thermal inertia, roughness fraction and geometric albedo here.

Figure 4 shows the contours of $\chi^2_{\rm r}(f_{\rm r}, \Gamma)$ according to Table 5, where the color variation from blue to red means increase of the reduced $\chi^2_{\rm r}$. The deep blue curve labeled by 1σ corresponds to $\Delta\chi^2_{\rm r} = 0.252$ from the minimum $\chi^2_{\rm r}$, constraining the scale of the free pa-

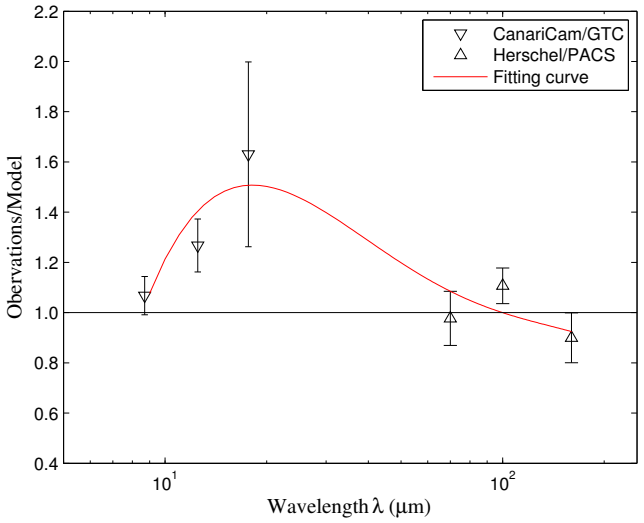

Fig. 2 The observation/model ratios as a function of wavelength for $\Gamma = 50\,\mathrm{J m^{-2}\,s^{-0.5}\,K^{-1}}$, $f_\mathrm{r} = 1.0$, $p_\mathrm{v} = 0.318$ and $D_\mathrm{eff} = 382\,\mathrm{m}$ when using $\epsilon(\lambda) \equiv 0.9$. The ratios with their errors at each wavelength are all error-weighted average results. The red fitting curve is obtained from a 4th degree polynomial fitting for $x = \log 10(\lambda)$, $y = F_\mathrm{obs}/F_\mathrm{model}$.

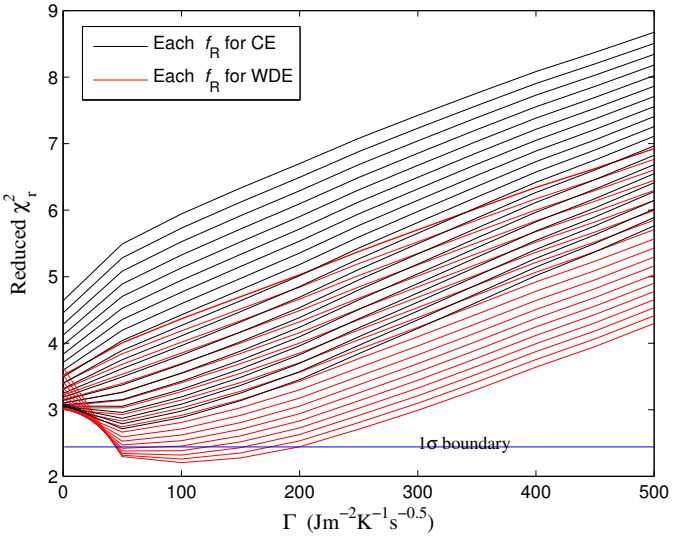

Fig. 3 $\Gamma \sim \chi^2_\mathrm{r}$ curves for both the CE and WDE cases considering $f_\mathrm{r} = 0.0 \sim 1.0$.

rameters with probability of about 68.3%, whereas the blue curve labeled by 3σ refers to $\Delta\chi^2_\mathrm{r} = 1.014$, giving the scale of free parameters with probability of about 99.73% (Press 2007).

Figure 5 shows the $p_\mathrm{v} \sim \chi^2_\mathrm{r}$ obtained in consideration of the above derived Γ and f_r as well as the absolute visual magnitude $H_\mathrm{v} = 19.09 \pm 0.19$, where 1σ and 3σ limits are the same as above. The scale of absolute visual magnitude H_v does not affect the distribution of reduced χ^2_r derived from each pair of thermal inertia and roughness fraction, but has significant influence on the corresponding geometric albedo and effective diameter. Thus we do not treat H_v as a free parameter, but consider its influence by only using the upper limit, mid-value and lower limit of H_v; each was adopted to be a constant in the fitting process. The final results of geometric albedo and effective diameter are constrained by considering three cases of H_v together, leading to the 1σ and 3σ scales being non-Gaussian.

Table 5 ATPM Fitting Results to Observations with WDE

Roughness	Thermal inertia Γ ($\mathrm{Jm^{-2}\,s^{-0.5}\,K^{-1}}$)																					
fraction	0		50		100		150		200		250		300		350		400		450		500	
f_{R}	p_{v}	χ^2_{r}	p_{v}	χ^2_{r}	p_{v}	χ^2_{r}	p_{v}	χ^2_{r}	p_{v}	χ^2_{r}	p_{v}	χ^2_{r}	p_{v}	χ^2_{r}	p_{v}	χ^2_{r}	p_{v}	χ^2_{r}	p_{v}	χ^2_{r}	p_{v}	χ^2_{r}
0.00	0.283	3.64	0.305	4.18	0.308	4.55	0.309	4.89	0.309	5.22	0.309	5.57	0.308	5.89	0.308	6.21	0.307	6.52	0.306	6.80	0.306	7.09
0.05	0.284	3.52	0.304	4.01	0.306	4.37	0.307	4.70	0.307	5.03	0.307	5.38	0.306	5.70	0.306	6.03	0.306	6.34	0.305	6.63	0.305	6.93
0.10	0.284	3.40	0.304	3.84	0.306	4.19	0.307	4.52	0.306	4.84	0.306	5.20	0.306	5.52	0.305	5.85	0.305	6.17	0.304	6.46	0.304	6.76
0.15	0.284	3.31	0.304	3.68	0.306	4.02	0.306	4.34	0.306	4.66	0.306	5.02	0.305	5.35	0.305	5.68	0.304	6.00	0.304	6.30	0.303	6.60
0.20	0.283	3.22	0.303	3.53	0.305	3.85	0.305	4.17	0.305	4.49	0.305	4.84	0.305	5.18	0.304	5.51	0.304	5.84	0.303	6.14	0.303	6.45
0.25	0.283	3.15	0.303	3.40	0.305	3.70	0.305	4.00	0.305	4.32	0.304	4.68	0.304	5.01	0.303	5.35	0.303	5.68	0.302	5.98	0.302	6.30
0.30	0.282	3.10	0.302	3.27	0.304	3.55	0.304	3.84	0.304	4.16	0.304	4.51	0.303	4.85	0.303	5.19	0.302	5.52	0.301	5.82	0.301	6.14
0.35	0.282	3.06	0.302	3.14	0.303	3.41	0.304	3.69	0.303	4.00	0.303	4.35	0.302	4.69	0.302	5.03	0.301	5.37	0.301	5.67	0.300	6.00
0.40	0.281	3.03	0.301	3.03	0.303	3.27	0.303	3.55	0.302	3.85	0.302	4.20	0.301	4.54	0.301	4.88	0.300	5.22	0.300	5.52	0.299	5.85
0.45	0.281	3.01	0.301	2.93	0.302	3.15	0.302	3.41	0.301	3.71	0.301	4.05	0.300	4.39	0.300	4.73	0.299	5.07	0.299	5.38	0.298	5.71
0.50	0.280	3.01	0.300	2.83	0.301	3.03	0.301	3.28	0.300	3.57	0.300	3.91	0.299	4.24	0.299	4.58	0.298	4.92	0.298	5.23	0.297	5.57
0.55	0.279	3.02	0.299	2.74	0.300	2.92	0.300	3.15	0.299	3.43	0.299	3.77	0.298	4.10	0.298	4.44	0.297	4.78	0.296	5.09	0.296	5.43
0.60	0.279	3.04	0.298	2.66	0.299	2.81	0.299	3.03	0.298	3.30	0.298	3.63	0.297	3.96	0.297	4.30	0.296	4.64	0.295	4.95	0.295	5.29
0.65	0.278	3.07	0.298	2.59	0.298	2.71	0.298	2.92	0.297	3.18	0.297	3.50	0.296	3.82	0.295	4.16	0.295	4.51	0.294	4.82	0.294	5.16
0.70	0.277	3.12	0.297	2.53	0.297	2.62	0.297	2.81	0.296	3.06	0.296	3.38	0.295	3.69	0.294	4.03	0.294	4.37	0.293	4.69	0.292	5.03
0.75	0.276	3.17	0.296	2.47	0.296	2.54	0.296	2.71	0.295	2.94	0.294	3.25	0.293	3.57	0.293	3.90	0.292	4.24	0.291	4.56	0.291	4.90
0.80	0.275	3.24	0.294	2.42	0.295	2.46	0.294	2.61	0.293	2.83	0.293	3.14	0.292	3.44	0.291	3.78	0.291	4.12	0.290	4.43	0.290	4.78
0.85	0.274	3.32	0.293	2.38	0.294	2.38	0.293	2.52	0.292	2.73	0.291	3.02	0.290	3.33	0.290	3.65	0.289	3.99	0.288	4.31	0.288	4.65
0.90	0.273	3.42	0.292	2.34	0.292	2.32	0.291	2.43	0.290	2.63	0.290	2.91	0.289	3.21	0.288	3.53	0.288	3.87	0.287	4.18	0.286	4.53
0.95	0.272	3.52	0.291	2.32	0.291	2.26	0.290	2.35	0.289	2.53	0.288	2.81	0.287	3.10	0.286	3.42	0.286	3.76	0.285	4.07	0.285	4.41
1.00	0.263	3.63	0.286	2.30	0.286	2.21	0.285	2.28	0.284	2.44	0.283	2.71	0.282	2.99	0.281	3.31	0.280	3.64	0.279	3.95	0.278	4.30

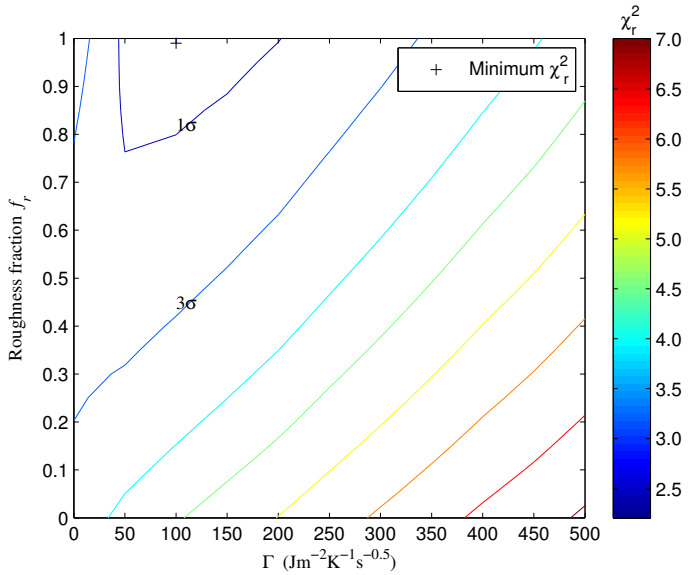

Fig. 4 $\chi^2_{\mathrm{r}}(f_{\mathrm{r}}, \Gamma)$ contours according to Table 5. The color (from blue to red) means increase of the profile for χ^2_{r}. 1σ corresponds to $\Delta\chi^2_{\mathrm{r}} = 0.252$ while 3σ corresponds to $\Delta\chi^2_{\mathrm{r}} = 1.014$ (Press 2007).

Using the assumed WDE in Table 4, we can derive thermal inertia Γ, roughness fraction f_{r}, geometric albedo p_{v} and effective diameter D_{eff}, where they are considered to be free parameters in the fitting procedure, on the likely 1σ and 3σ scales. We summarize the relevant results in Table 6.

4 DISCUSSION AND CONCLUSIONS

In this work, the mid-IR and far-IR data of Apophis observed by CanariCam on Gran Telescopio CANARIAS and PACS on Herschel are analyzed by the ATPM, where four parameters, including thermal emissivity, thermal

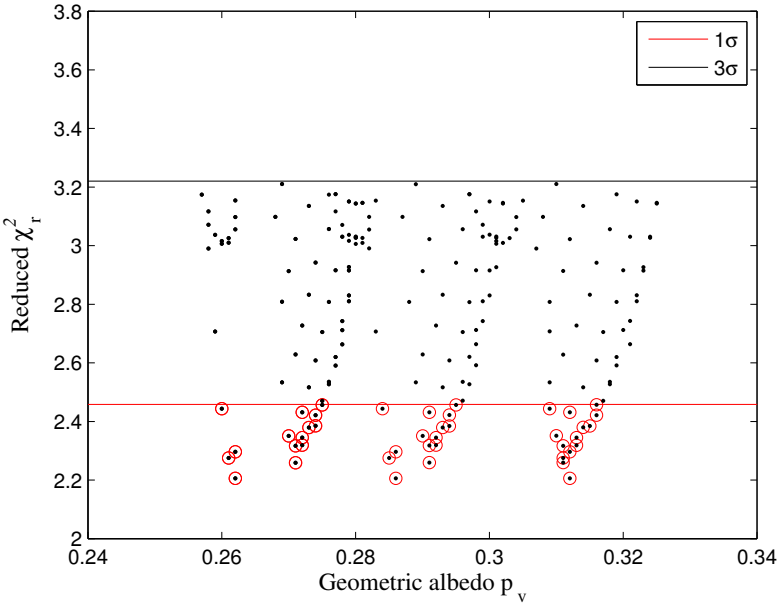

Fig. 5 $p_{\rm v} \sim \chi^2_{\rm reduced}$ profiles fit to the observations in consideration of the derived 1σ and 3σ range for $f_{\rm r}$ and Γ and the absolute visual magnitude $H_{\rm v} = 19.09 \pm 0.19$.

Table 6 The Derived Parameters for Apophis

Properties	1σ scale	3σ scale
Thermal inertia Γ($\mathrm{Jm^{-2}\,s^{-0.5}\,K^{-1}}$)	100^{+100}_{-52}	100^{+240}_{-100}
Roughness fraction $f_{\rm r}$	0.78∼1.0	0.2∼1.0
Geometric albedo $p_{\rm v}$	$0.286^{+0.03}_{-0.026}$	$0.286^{+0.039}_{-0.029}$
Effective diameter $D_{\rm eff}$ (m)	378^{+19}_{-25}	378^{+27}_{-29}

inertia, roughness fraction and geometric albedo, are investigated. We found that the thermal emissivity of Apophis should be wavelength dependent, and using a similar emissivity like that of Vesta could obtain a better fitting. As a result, we derive the thermal inertia, roughness fraction, geometric albedo and effective diameter of Apophis in a possible 1σ scale of $\Gamma = 100^{+100}_{-52}\,\mathrm{Jm^{-2}\,s^{-0.5}\,K^{-1}}$, $f_{\rm r} = 0.78 \sim 1.0$, $p_{\rm v} = 0.286^{+0.030}_{-0.026}$ and $D_{\rm eff} = 378^{+19}_{-25}\,\mathrm{m}$, and 3σ scale of $\Gamma = 100^{+240}_{-100}\,\mathrm{Jm^{-2}\,s^{-0.5}\,K^{-1}}$, $f_{\rm r} = 0.2 \sim 1.0$, $p_{\rm v} = 0.286^{+0.039}_{-0.029}$ and $D_{\rm eff} = 378^{+27}_{-29}\,\mathrm{m}$. The derived thermal inertia supports the result of Licandro et al. (2016) despite being a little lower. The best fit high roughness is different from the result of Licandro et al. (2016), but is inconsistent with the work of Müller et al. (2014) where the best fit solution also supports a high roughness.

To verify the reliability of our fitting procedure and derived outcomes, we employ the ratio of 'observation/model' (Müller et al. 2005, 2011, 2012) to examine how these theoretical model results match the observations at various wavelengths (see Fig. 6).

In Figure 6, the observation/model ratios are shown at each observational wavelength for $f_{\rm r} = 1.0$, $\Gamma = 100\,\mathrm{Jm^{-2}\,s^{-0.5}\,K^{-1}}$, $p_{\rm v} = 0.286$ and $D_{\rm eff} = 378\,\mathrm{m}$. The ratios are distributed more nearly around 1.0 compared to Figure 2, despite the ratios at $17.65\,\mu\mathrm{m}$ becoming larger than unity which again support the idea that Apophis' spectral emissivity should be wavelength dependent. However, we cannot know exactly how the spectral emissivity varies with wavelength at present, for the available spectral data are not enough. If, in the future, more spectral data observed from mid-IR to far-IR are obtained, we may find out how the emissivity of Apophis depends on wavelength.

Given the low gravitational acceleration on the surface of asteroids, it was generally thought that regolith formation would not be possible, especially on small-size asteroids. The statistical results of thermal inertia versus the size of asteroids in the work of Delbo' et al. (2007) suggest that small-size asteroids should have high thermal inertia, indicating a rocky surface, also supporting the above idea. However, regolith on the small-size asteroid Itokawa was detected by the Hayabusa spacecraft (Saito et al., 2006), which suggests that regolith formation on asteroids, even small-size asteroids, is also possible. The low thermal inertia result of Apophis in this work somewhat adds support to the idea that regolith formation may not be dominated by the size of an asteroid. If a small asteroid has experienced a sufficiently long

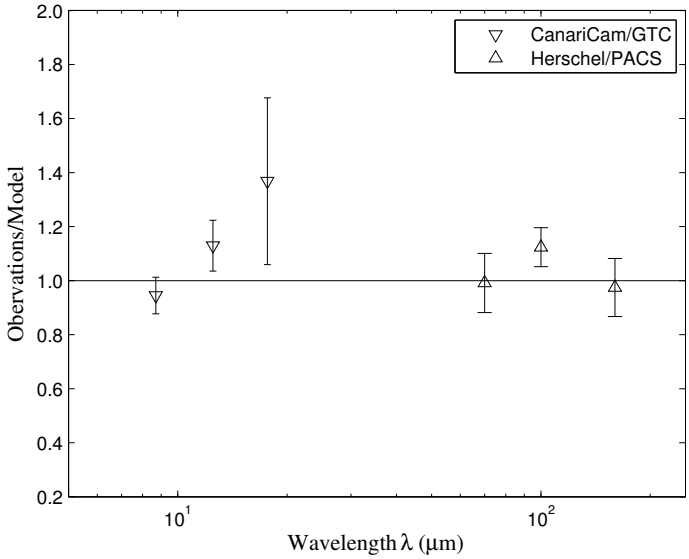

Fig. 6 The observation/model ratios as a function of wavelength for $\Gamma = 100\ \mathrm{Jm^{-2}\ s^{-0.5}\ K^{-1}}$, $f_\mathrm{r} = 1.0$, $p_\mathrm{v} = 0.286$ and $D_\mathrm{eff} = 378\,\mathrm{m}$ in consideration of WDE. The ratios with their errors at each wavelength are all error-weighted average results.

process of space weathering, the presence of regolith should be also reasonable. On the other hand, the size of Apophis is similar to that of asteroid Itokawa, indicative of a similar dynamical lifetime in principle. But the derived thermal inertia of Apophis is much lower than the observed thermal inertia of Itokawa (Müller et al. 2005), indicating Apophis may actually either have existed for a longer lifetime or experience stronger space weathering but weak reoligth migration on its surface, causing more dust to be produced and retained. We notice that Apophis has much slower rotation, $P_\mathrm{rot} \approx 30.56\,\mathrm{h}$, than Itokawa ($P_\mathrm{rot} \approx 12.13\,\mathrm{h}$), which may account for Apophis' lower thermal inertia, for the produced dust should more easily accumulate on a slowly-rotating asteroid.

Generally, a rough surface would generate stronger Yarkovsky orbit drift than a smooth surface (Rozitis & Green 2012). Thus the Yarkovsky effect that induced a decreasing rate of Apophis' semimajor axis should be even larger than the predicted value of Vokrouhlický et al. (2015), because our results show Apophis tends to have a rough surface, which should be taken into account to predict its orbit movement. In addition, it is possible that Apophis may be one of Vesta's fragments delivered from the Main Belt by the Yarkovsky effect, in consideration of its long existence time suggested by low thermal inertia, and similar surface properties to Vesta implied by albedo and thermal emissivity.

In conclusion, when we attempt to investigate surface thermophysical properties of a target asteroid by utilizing the thermal IR radiometric method to fit observed data from mid-IR to far-IR, CE may not always be the best choice. For asteroid Apophis, the combined data of mid-IR from CanariCam and far-IR from Herschel reveal possible wavelength dependent thermal emissivity from $8.70\ \mu\mathrm{m}$ to $160\ \mu\mathrm{m}$, where the maximum emissivity may appear around $20\ \mu\mathrm{m}$ like that of Vesta, because this kind of emissivity can achieve a better degree of fitting through the use of ATPM. Moreover, the derived results of low thermal inertia $\Gamma = 100^{+240}_{-100}\,\mathrm{Jm^{-2}\,s^{-0.5}\,K^{-1}}$ and high roughness fraction $f_\mathrm{r} = 0.2 \sim 1.0$ indicate that Apophis may have experienced a long process of space weathering, but less regolith migration, enabling the produced dust to stay on its surface. These new deductions would be important for predicting Apophis' orbital movement and potential Earth impact probability so as to establish an artificial mechanism to avoid the probable impact.

Acknowledgements We thank the anonymous referee for their insightful comments and suggestions that helped to improve the manuscript. This work is financially supported by the National Natural Science Foundation of China (Grant Nos. 11473073, 11403105, 11633009 and 11661161013), the Science and Technology Development Fund of Macau (Grant Nos. 039/2013/A2 and 017/2014/A1), the innovative and interdisciplinary program by CAS (Grant No. KJZD-EW-Z001), the Natural Science Foundation of Jiangsu Province (Grant No. BK20141509) and the Foundation of Minor Planets of Purple Mountain Observatory.

References

Abe, S., Mukai, T., Hirata, N., et al. 2006, Science, 312, 1344

Binzel, R. P., Rivkin, A. S., Thomas, C. A., et al. 2009, Icarus, 200, 480

Bottke, Jr., W. F., Vokrouhlický, D., Rubincam, D. P., & Nesvorný, D. 2006, Annual Review of Earth and Planetary Sciences, 34, 157

Bowell, E., Hapke, B., Domingue, D., et al. 1989, in Asteroids II, ed. R. P. Binzel, T. Gehrels, & M. S. Matthews, 524

Chesley, S. R. 2006, in IAU Symposium, 229, Asteroids, Comets, Meteors, ed. L. Daniela, M. Sylvio Ferraz, & F. J. Angel, 215

Delbo', M., dell'Oro, A., Harris, A. W., Mottola, S., & Mueller, M. 2007, Icarus, 190, 236

Farnocchia, D., Chesley, S. R., Chodas, P. W., et al. 2013, Icarus, 224, 192

Fowler, J. W., & Chillemi, J. R. 1992, IRAS Asteroids Data Processing. In The IRAS Minor Planet Survey, 17

Fujiwara, A., Kawaguchi, J., Yeomans, D. K., et al. 2006, Science, 312, 1330

Gilmore, A. C., Kilmartin, P. M., Young, J., et al. 2004, Minor Planet Electronic Circulars, 2004-Y25

Giorgini, J. D., Benner, L. A. M., Ostro, S. J., Nolan, M. C., & Busch, M. W. 2008, Icarus, 193, 1

Licandro, J., Müller, T., Alvarez, C., Alí-Lagoa, V., & Delbo, M. 2016, A&A, 585, A10

Mueller, T. G., & Lagerros, J. S. V. 1998, A&A, 338, 340

Müller, T. G., Sekiguchi, T., Kaasalainen, M., Abe, M., & Hasegawa, S. 2005, A&A, 443, 347

Müller, T. G., Ďurech, J., Hasegawa, S., et al. 2011, A&A, 525, A145

Müller, T. G., O'Rourke, L., Barucci, A. M., et al. 2012, A&A, 548, A36

Müller, T. G., Kiss, C., Scheirich, P., et al. 2014, A&A, 566, A22

Pravec, P., Scheirich, P., Ďurech, J., et al. 2014, Icarus, 233, 48

Press, W. H. 2007, Numerical Recipes, The Art of Scientific Computing (3rd edn.; Cambridge: Cambridge Univ. Press)

Rozitis, B., & Green, S. F. 2011, MNRAS, 415, 2042

Rozitis, B., & Green, S. F. 2012, MNRAS, 423, 367

Saito J., Miyamoto H., Nakamura R. et al. Science, 2006, 312, 1341

Thuillot, W., Bancelin, D., Ivantsov, A., et al. 2015, A&A, 583, A59

Vokrouhlický, D., Farnocchia, D., Čapek, D., et al. 2015, Icarus, 252, 277

Wang, N., Peng, Q. Y., Zhang, X. L., et al. 2015, MNRAS, 454, 3805

Yu, L., Ji, J., & Wang, S. 2014, MNRAS, 439, 3357

Yu, L. L., & Ji, J. H., 2015, MNRAS, 452, 368